

Article

A Fluid Inclusion and Critical/Rare Metal Study of Epithermal Quartz-Stibnite Veins Associated with the Gerakario Porphyry Deposit, Northern Greece

Christos L. Stergiou ¹, Vasilios Melfos ^{1,*}, Panagiotis Voudouris ², Lambrini Papadopoulou ¹, Paul G. Spry ³, Irena Peytcheva ⁴, Dimitrina Dimitrova ⁴ and Elitsa Stefanova ⁴

¹ Faculty of Geology, Aristotle University of Thessaloniki, 54124 Thessaloniki, Greece; christer@geo.auth.gr (C.L.S.); lambrini@geo.auth.gr (L.P.)

² Faculty of Geology and Geoenvironment, National and Kapodistrian University of Athens, 15784 Athens, Greece; voudouris@geol.uoa.gr

³ Department of Geological and Atmospheric Sciences, Iowa State University, Ames, IA 50011-1027, USA; pgspry@iastate.edu

⁴ Geological Institute, Bulgarian Academy of Sciences, 241113 Sofia, Bulgaria; irena.peytcheva@erdw.ethz.ch (I.P.); didi@geology.bas.bg (D.D.); elitsas@intern.ethz.ch (E.S.)

* Correspondence: melfosv@geo.auth.gr



Citation: Stergiou, C.L.; Melfos, V.; Voudouris, P.; Papadopoulou, L.; Spry, P.G.; Peytcheva, I.; Dimitrova, D.; Stefanova, E. A Fluid Inclusion and Critical/Rare Metal Study of Epithermal Quartz-Stibnite Veins Associated with the Gerakario Porphyry Deposit, Northern Greece. *Appl. Sci.* **2022**, *12*, 909. <https://doi.org/10.3390/app12020909>

Academic Editors: Adam Piestrzyński and Stanisław Z. Mikulski

Received: 20 December 2021

Accepted: 12 January 2022

Published: 17 January 2022

Publisher's Note: MDPI stays neutral with regard to jurisdictional claims in published maps and institutional affiliations.



Copyright: © 2022 by the authors. Licensee MDPI, Basel, Switzerland. This article is an open access article distributed under the terms and conditions of the Creative Commons Attribution (CC BY) license (<https://creativecommons.org/licenses/by/4.0/>).

Abstract: The Gerakario Cu-Au porphyry deposit in the Kilkis ore district, northern Greece, contains epithermal quartz-stibnite veins on the eastern side of the deposit, which crosscut a two-mica gneiss. Metallic mineralization in these veins consists of stibnite + berthierite + native antimony + pyrite + arsenopyrite, and minor marcasite, pyrrotite, chalcopyrite, löllingite, and native gold. Bulk geochemical analyses of the ore reveal an enrichment in critical and rare metals, including Ag, Au, Bi, Ce, Co, Ga, La, and Sb. Analysis of stibnite with LA-ICP-MS showed an enrichment in base metals (As, Cu, Pb), as well as weak to moderate contents of critical and rare metals (Ag, Bi, Ce, La, Re, Sm, Th, Ti, Tl). A statistical analysis of the trace elements show a positive correlation for the elemental pairs Ce-La, Ce-Sb, and La-Sb, and a negative correlation for the pair Bi-Sb. Fluid inclusions in the A-type veins of the porphyry-style mineralization show the presence of fluid boiling, resulting in a highly saline aqueous fluid phase (35.7 to 45.6 wt.% NaCl equiv.) and a moderately saline gas phase (14 to 22 wt.% NaCl equiv.) in the system H₂O-NaCl-KCl at temperatures varying between 380° and 460 °C and pressures from 100 to 580 bar. Mixing of the moderate saline fluid with meteoric water produced less saline fluids (8 to 10 wt.% NaCl equiv.), which are associated with the epithermal quartz-stibnite vein mineralization. This process took place under hydrostatic pressures ranging from 65 to 116 bar at a depth between 600 and 1000 m, and at temperatures mainly from 280° to 320 °C.

Keywords: rare metals; critical metals; rare earth elements; stibnite; epithermal veins; Gerakario; Kilkis ore district; Serbo-Macedonian metallogenic province; mineral chemistry; fluid-inclusions

1. Introduction

Critical raw materials (CRM) are integral components of a resilient and sustainable economy and society [1,2]. The 2020 European Union CRM list comprises the metals: Be, Bi, Co, Ga, Ge, Hf, In, Li, Nb, Sb, Sc, Sr, Ta, Ti, V, and W, as well as the group of rare earth elements (REE) and platinum group elements (PGE) [3]. A sustainable supply of mineral raw materials needs accessible deposits and efficiently productive mines [4]. Advances in ore exploration further contribute to achieving this supply chain.

Alkaline- to peralkaline-carbonatite igneous rocks, sedimentary uranium and phosphorite ores, and placer-type REE deposits are the main sources for critical and rare metals [5–7]. The exploitation of critical and rare metals mainly as by-products from porphyry-epithermal systems could support this effort [8,9].

Porphyry Cu-Au-Mo deposits are potential exploration and exploitation targets for critical and rare metals, as they exhibit enrichments in Re, Te, Co, Bi, U, and PGE [10]. The polymetallic assemblages found in the periphery of porphyry systems related to skarn, replacement, vein, and intermediate sulfidation epithermal mineralization types are enriched in Mn, Ge, Ga, In, Bi, Sb, As, W, and Te [10]. In addition, low- to high-sulfidation epithermal overprints of porphyry systems may include Te, Bi, As, Sb, V, and F [10,11]. However, the enrichment processes of these metals and their distribution require further investigation. Bulk geochemistry and mineral chemistry of hydrothermal alterations and ore mineralization can assist in this effort. In addition, the metallic minerals hosted in porphyry-epithermal deposits could be associated with varying amounts of critical and rare metals incorporated as: (1) solid solution or nanoparticles in the crystal lattice, (2) nano-scale mineral inclusions, and (3) visible micro- to macro-scale minerals [12–16]. These inclusions can be formed through direct precipitation from multi-stage hydrothermal fluids into the minerals, or from processes, such as overgrowth and recrystallization, leading to exsolution, remobilization, and resorption of trace elements [12,14].

Antimony is a CRM and is fundamental to the aerospace-defense, textiles, mobility-automotive, and construction industrial ecosystems, as it is used in defense applications (e.g., ammunition, optics, laser sighting), flame retardants, and lead-acid batteries [3]. Stibnite (Sb_2S_3) commonly occurs in magmatic-hydrothermal mineralization and is the principal ore mineral in Sb deposits [17,18]. Major stibnite ores are found in the Xiangzhong metallogenic province in China (>50% of global Sb production and reserves) [16]. They include structurally controlled vein-style mineralization related to distal intrusions, which are hosted in sedimentary or metamorphic rocks [16]. Additionally, antimony and stibnite are also accommodated in epithermal vein-type mineralization and in sediment-hosted distal-disseminated mineralization found in the periphery of porphyry systems [10,19]. Trace elemental composition of stibnite remains largely unexplored [16]. Copper, Pb, and As are the main lattice bound substitutions for Sb in stibnite (in wt.% level), whereas Au, Ag, Bi, In, Mo, Sn, Co, Cr, V, Zn, Ni, Ga, Ge, Rb, Sr, Pd, Cd, and U can be incorporated in minor amounts (ppm level), related to nano-scale mineral inclusions [16]. These inclusions comprise a range of low temperature sulfides, sulfosalts, and arsenides (e.g., marcasite, chalcopyrite, löllingite, berthierite, galena) [20]. Stibnite may also be enriched in REEs, especially in light REEs, such as Ce and La [21].

Europe has a long history in mineral raw materials exploitation. However, the European Union (EU) largely relies on imports of CRM [12]. Despite their high potential, large areas of Europe, including northern Greece, remain underexplored for ore deposits using modern exploration methods [22–24].

The Kilkis ore district in northern Greece belongs in the Vertiskos unit and is part of the Serbo-Macedonian metallogenic province that is a potential region for future exploration projects targeting critical and rare metals [25–33] (Figure 1). This district hosts Cenozoic deposits and prospects enriched in Cu and Au, as well as in critical and rare metals (e.g., Sb, W, Te, Bi, Ga, Co, Ag, and REE) [25–33]. Oligocene to Miocene porphyry deposits (Vathi, Gerakario, Pontokerasia, Koryfi, Doirani) are clustered in the northern part of the district [23,24,32,33]. Ancient mining galleries indicate the importance of these mineralization for gold and copper during antiquity. Several other deposits, including skarn/carbonate replacement, epithermal and vein type mineralization in metamorphic rocks are found proximal or distal to magmatic intrusions, at the central and southern parts of the Vertiskos unit, as well as in the adjacent Kerdylion unit [23,24,32,33] (Figure 1). For deposits distal to magmatic rocks, the regional metallogenic model, the local structural setting, the character of the hydrothermal fluids, and their ore geochemistry (i.e., enrichments in chalcophile elements, such as Au, Bi, Co, Te) relate their genesis to a combination of factors, including the relationship to buried magmatic intrusions, shear zones, and brittle deformation [23,34,35].

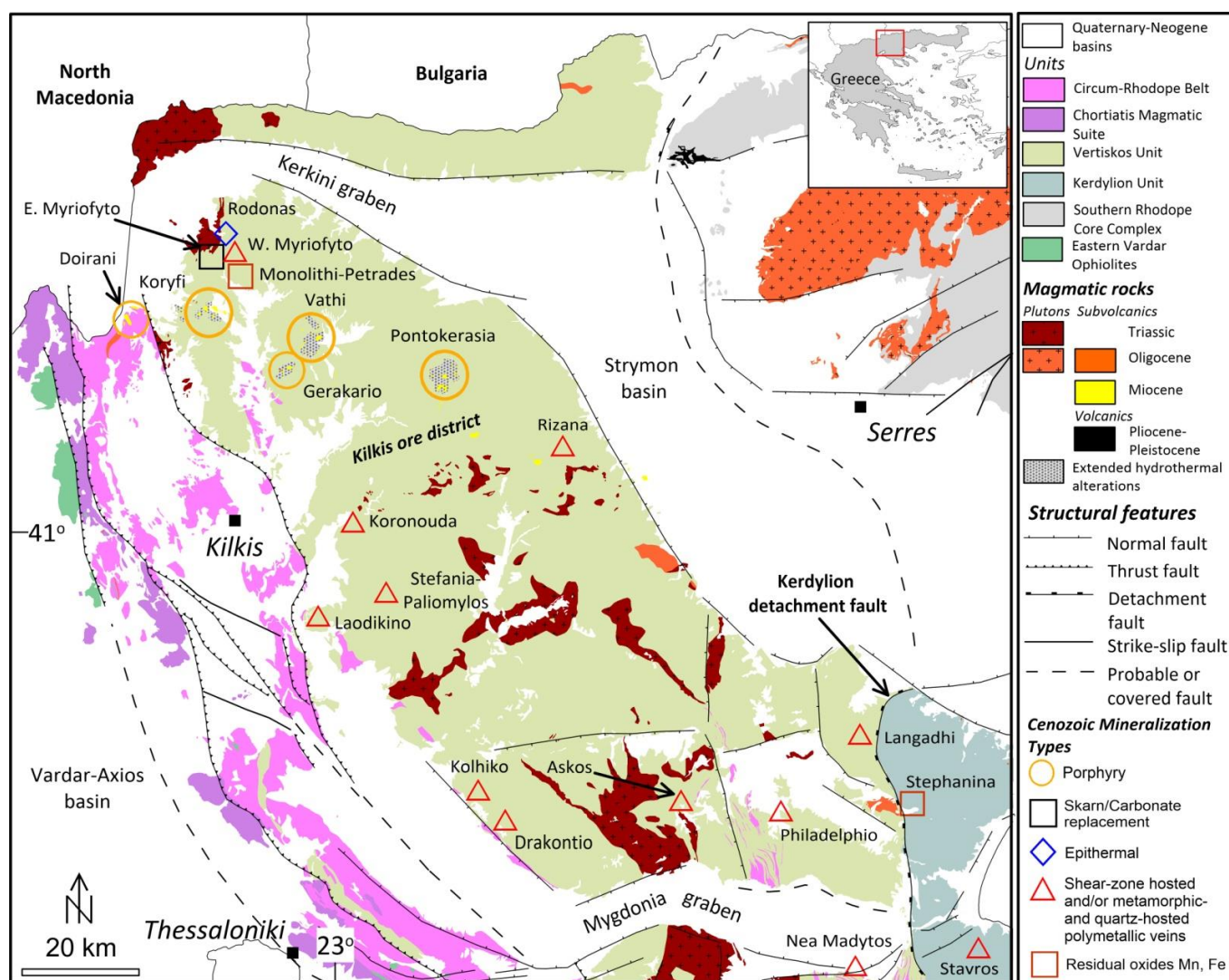


Figure 1. Geological setting of the Cenozoic magmatic rocks and the related ore types in the Kilis ore district, northern Greece (modified after References [23,24,31–33]). The studied area in Gerakario is also shown.

The most important Sb deposits in the region are found at Rizana, Philadelphio, and Gerakario [23,31,32] (Figure 1). The Rizana (also known as Lachanas) shear-zone hosted deposit is found in sheeted quartz veins crosscutting two-mica gneiss and schist of the Vertiskos unit [28,36–38]. Sericitization and silicification are observed in the basement rocks [36]. The ore mineralization is enriched in Sb and W and the ore assemblage includes stibnite, wolframite, sphalerite, pyrite, and berthierite, and traces of chalcopryrite, arsenopyrite, marcasite, and native antimony, arsenic, and gold [36,37]. Gangue minerals are quartz and barite, while alteration minerals include quartz, sericite, chlorite, calcite, and dolomite [36]. Between the 1930s and 1950s, 9000 tons of stibnite ore, with up to 40% of Sb in the produced concentrate, were extracted from underground mines [28]. Wolframite was also mined between the 1910s and 1940s. The measured reserves of stibnite (0.3 wt.% Sb in average) are 5000 t, and the indicated reserves vary between 50,000 and 100,000 t, including also 1000 t of wolframite [28].

At Philadelphio, Sb mineralization occurs in shear-zone hosted massive and discordant stibnite veins, crosscutting the metamorphic rocks of the Vertiskos unit [29] (Figure 1). Hydrothermal alterations include sericitization and chloritization of the host rocks [22]. The ore assemblage consists of stibnite, arsenopyrite, chalcopryrite, chalcostibite, traces of scheelite, kermesite, marcasite, pyrite, pyrrhotite, sphalerite, stibiconite, tetrahedrite,

covellite, wolframite, zinkenite, melnikovite, and native gold, while quartz is the gangue mineral [22]. Indicated resources include 10.08 Mt of ore, grading 3.36 wt.% of Sb [22].

The Gerakario area has been explored for Cu, Au, Mo, and base metals between the 1970s and the 1990s [39]. The exploration of the Cu-Au porphyry deposit included soil geochemistry, geophysical surveys, and drilling [39,40]. Stibnite is hosted in quartz veins found at the periphery of the porphyry deposit. Stibnite was mined in the 1930s with underground galleries and wells, but the amount of the extracted ore is unknown. Probable and indicated reserves are up to 0.13 Mt of ore, grading 0.3% Cu and 1.4 g/t Au for the porphyry deposit [28]. Estimations on Sb resources and reserves are yet to be determined. In the present study, we investigate the distribution of the critical and rare metals in the Gerakario deposit, with bulk geochemical analysis of the quartz-stibnite veins and trace elemental analysis of stibnite by laser ablation inductively coupled plasma mass spectrometry (LA-ICP-MS). Emphasis is given on the elements: Ag, Au, Bi, Cd, Ce, Co, Ga, Gd, Ge, Hg, In, La, Nb, Nd, Re, Sb, Se, Sm, Ta, Te, Th, Ti, U, V, and W. Then, we evaluate the distribution of the critical and rare metals in stibnite by applying Pearson's correlation. Finally, on the basis of the microthermometric data collected from the A-type veins (porphyry stage) and the quartz-stibnite veins (epithermal stage), we reconstruct the history of the ore-related fluid evolution history. The results provide new data on the critical and rare metals endowment of the quartz-stibnite epithermal veins and a genetic model of the Gerakario porphyry-epithermal system.

2. Geological Setting and Mineralization

2.1. Local Geology

Paleozoic to Mesozoic two-mica gneisses, serpentized peridotites, and amphibolite of the Vertiskos unit form the basement rocks in the Gerakario area (Figure 2). Towards the east, Triassic meta-sedimentary rocks of the Circum-Rhodope belt were obducted onto the Vertiskos unit (Figure 2). Cenozoic plutonic to subvolcanic rocks occur at Gerakario [41], with the plutonic rocks consisting mainly of granodiorites (34 ± 0.5 Ma; U-Pb zircon ages [42]), which appear as small stocks that are silica-saturated with calc-alkaline affinities [41]. According to Frei [42], subvolcanic rocks include stocks and dikes of syenite (22 ± 0.8 Ma; U-Pb zircon ages) and diorite (24.7 ± 1.3 Ma; K-Ar whole rock [43]), which locally exhibit porphyritic textures. They are silica saturated with slightly alkaline affinities [42]. Outcrops of phreatic breccias are found in the broader area intruding the basement rocks [39]. Local structures include NE-SW and E-W trending normal to oblique faults, which crosscut the syenite [41] (Figure 2). The granodiorite consists of quartz, plagioclase, hornblende, and biotite, with minor K-feldspar, zircon, apatite, and titanite [42]. The alteration assemblages include biotite (weak potassic alteration), calcite, chlorite, and epidote (propylitic alteration), and sericite (sericitic alteration) [42]. The syenite comprises quartz, plagioclase, K-feldspar, biotite, and hornblende, and minor zircon, apatite, rutile, and titanite in a groundmass of quartz and K-feldspar [42]. Alteration assemblages include biotite, magnetite, and K-feldspar (potassic alteration), chlorite, allanite, and calcite (propylitic alteration), and sericite and quartz (sericitic alteration) [42]. Hydrothermal alterations are largely superimposed on each other and have significantly altered both the magmatic rocks and the surrounding metamorphic rocks [39]. Approximately 4 km northeast of Gerakario, the Vathi Cu-Au \pm Mo porphyry deposit is enriched in Ag, Au, Bi, Co, Se, and Te, as well as in REE (Ce, Gd, La, Nd, and Sm) [32,33] (Figure 1). In addition, minor mineralized veins are found in the adjacent metamorphic rocks, consisting mainly of pyrite and chalcopyrite (\pm arsenopyrite, galena, stibnite) [39] (Figure 2).

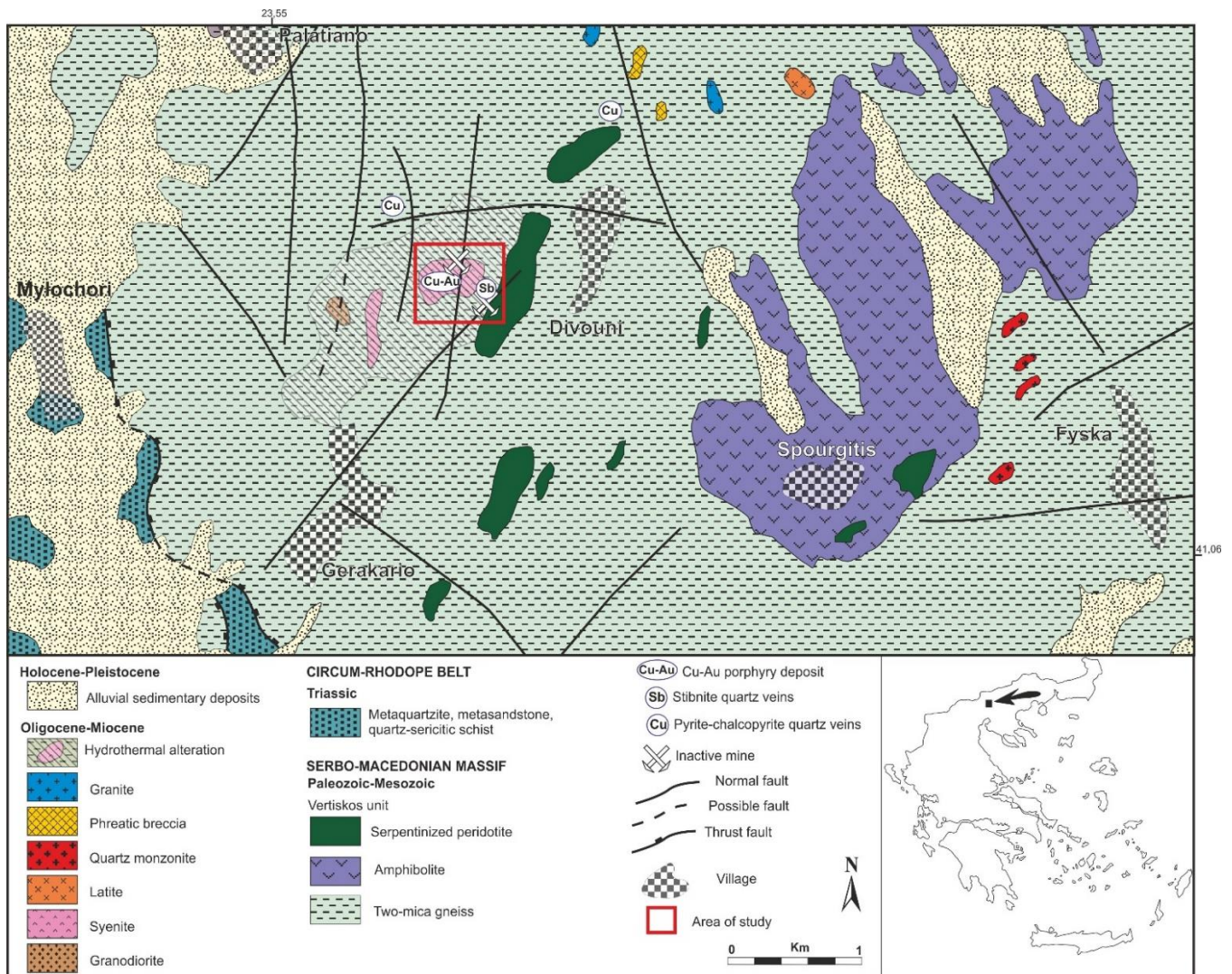


Figure 2. Geological map of the Gerakario showing the Cu-Au porphyry system and the stibnite-quartz veins (modified after Miggiros et al. [41]).

2.2. Porphyry Cu-Au Mineralization

The porphyry mineralization at Gerakario (N 41.117023°, E 22.929289°) is genetically associated with syenite and hosted in syenite, granodiorite, and the surrounding metamorphic rocks [39]. Ore textures include disseminations and A- and D-type veins [39]. According to Frei [42], the porphyry type mineralization is found as disseminations with pyrite-chalcocopyrite, and stockworks of A-type veins with magnetite-pyrite-chalcocopyrite, spatially associated to potassically altered syenite. In addition, disseminations and D-type veins with pyrite and minor chalcocopyrite are found in the sericitic alteration, which also affected the syenite, the granodiorite, and the metamorphic rocks [39,43]. The gneiss in contact with the syenite is strongly sheared and extensively altered [39]. Near the surface, the porphyry mineralization is significantly oxidized. In the oxidation zone, pyrite was replaced by goethite and jarosite, chalcocopyrite by malachite, and magnetite by hematite [39,43,44].

2.3. Epithermal Sb Mineralization

In the eastern part of the porphyry system, Sb-rich mineralization (N 41.114297°, E 22.935334°) is hosted in epithermal quartz veins crosscutting the two-mica gneiss (Figures 2 and 3a). The quartz-stibnite veins are continuous, up to 10 cm in width, and locally branched. They consist of massive stibnite with minor of berthierite, native anti-

mony, pyrite, and arsenopyrite (Figure 3b–d). Traces of marcasite, pyrrhotite, chalcopyrite, löllingite, and native gold are also present [45]. Gangue minerals include quartz and minor calcite. Traces of valentinite (Sb_2O_3) are related to supergene oxidation. Stibnite is the predominant ore mineral in the epithermal quartz veins (<5 cm in width) (Figure 3b). Quartz and calcite occur on the walls of the epithermal veins, and as veinlets (<2 cm in width) with traces of stibnite. A spatially limited hydrothermal halo consisting primarily of sericite is observed in the surrounding two-mica gneiss.

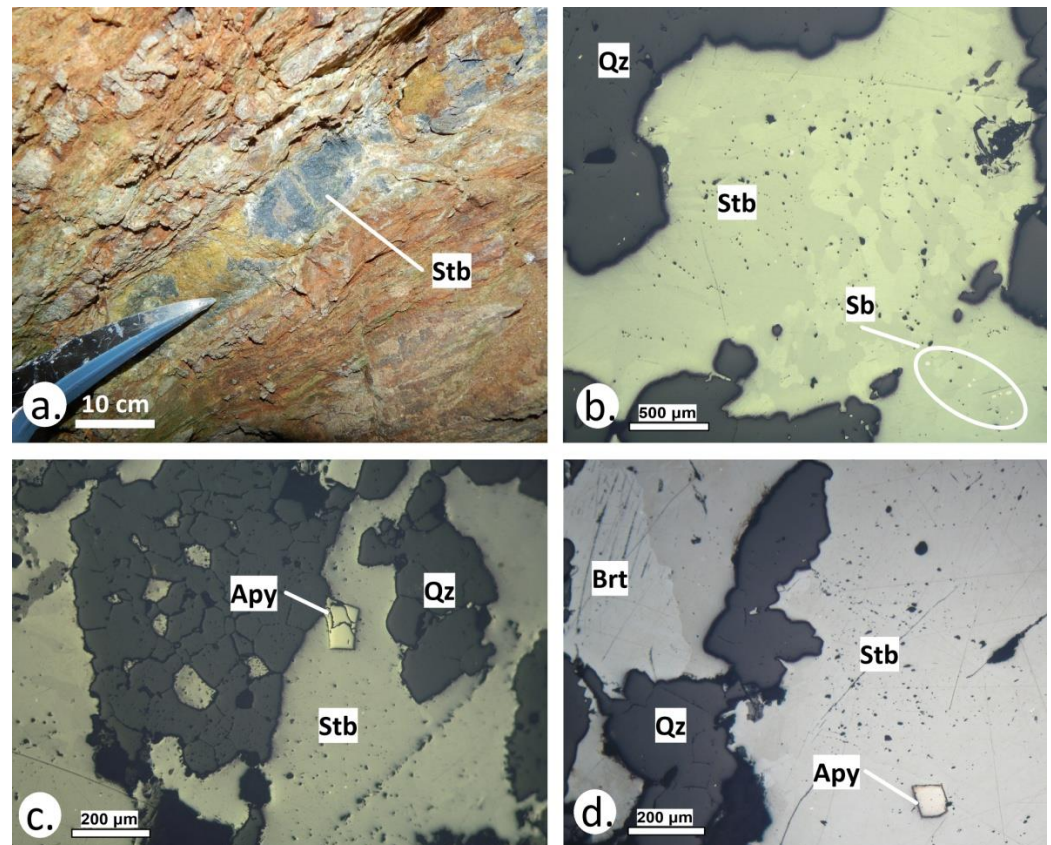


Figure 3. Stibnite from the epithermal vein-type Sb mineralization at Gerakario (photomicrographs in plane-polarized reflected light: (b–d)). (a) Epithermal quartz vein with massive stibnite (Stb), crosscutting the gneiss (b). Stibnite (Stb), and native antimony (Sb) with quartz (Qz). (c) Euhedral arsenopyrite (Apy) in stibnite (Stb) with quartz (Qz). (d) Euhedral arsenopyrite (Py) in stibnite (Stb), and berthierite (Brt) with quartz (Qz).

3. Materials and Methods

3.1. Fieldwork and Sampling

Fourteen samples (Ger 1 to Ger 14) were collected from the hydrothermally altered syenite and the surrounding metamorphic rocks at Gerakario. The sampling targeted the A-veins related to the porphyry system. In addition, eight samples (Ger 15 to Ger 22) were collected from the epithermal quartz-stibnite veins in the underground galleries.

3.2. Microscopy

Optical microscopy study was done at the Department of Mineralogy-Petrology-Economic Geology, Aristotle University of Thessaloniki (AUTH). In total, 15 polished sections were prepared and studied using a Leitz LaborLux 11 Pol dual reflected-transmitted light polarizing microscope (Leica Microsystems, Wetzlar, Germany) coupled.

3.3. Bulk Chemical Analysis

Trace element bulk geochemical analysis, including REEs, was conducted by inductively coupled plasma atomic emission spectroscopy (ICP-AES) by dissolving samples in Aqua Regia. The geochemical analyses were carried out at MSALABS, Langley, BC, Canada. The full dataset is given in Table S1.

3.4. Scanning Electron Microscope

The polished sections were studied with a JEOL JSM-840A scanning electron microscope (SEM) (JEOL Ltd., Tokyo, Japan) equipped with an OXFORD INCA 300 energy-dispersive system (EDS) (Oxford Instruments Ltd., Abingdon, UK) at the Faculty of Sciences, AUTH. The operating conditions were a 20 kV accelerating voltage and 0.4 mA probe current, 80s analysis time, and a beam diameter of $\sim 1 \mu\text{m}$, in the back-scattering electron (BSE) mode. Internal empirical corrections were performed to compensate for peak overlap. SEM-EDS micro-analysis was targeted on the mineral chemistry of stibnite and on the minerals found as micro-scale inclusions in it. Additionally, the antimony content was used as an internal standard in LA-ICP-MS analyses for stibnite. The average values of the conducted SEM-EDS analyses are given in Table S2.

3.5. LA-ICP-MS

Following electron microscopy study, two polished sections from the stibnite mineralization were analyzed by LA-ICP-MS. Trace element concentrations in stibnite were measured using a PerkinElmer ELAN DRC-e ICP (PerkinElmer Inc., Waltham, MA, USA) mass spectrometer combined with a New Wave UP193-FX excimer laser ablation system (New Wave Research, Inc., Fremont, CA, USA) at the Geological Institute, Bulgarian Academy of Sciences, Sofia, Bulgaria. The ablation was conducted in He medium. In order to maximize sensitivity, the ICP-MS was optimized daily with respect to the oxide production rate of ThO/Th (0.5%). Operating conditions of the laser system include 5 Hz repetition rate, 35 μm spot size, and energy density on analyzed minerals and standards of 5.0 to 5.2 J/cm². The nebulizer gas flow rate was 0.8 L/min, while auxiliary and make-up gas flows rates were 0.92 L/min. The analysis time was 100 s (background: 40 s, laser-on the sample: 60 s). The acquisition dwell time was set to 0.02 s for ⁷⁴Ge, ⁸²Se, ¹¹⁵In, ¹²⁵Te, and ²⁰²Hg, to 0.03 s for ¹⁰⁷Ag, to 0.04 s for ¹⁹⁷Au, and to 0.01 s for all other elements. The monitored isotopes include: ²⁷Al, ³¹P, ³⁴S, ⁴⁹Ti, ⁵¹V, ⁵³Cr, ⁵⁵Mn, ⁵⁷Fe, ⁵⁹Co, ⁶⁰Ni, ⁶⁵Cu, ⁶⁶Zn, ⁷¹Ga, ⁷³Ge, ⁷⁴Ge, ⁷⁵As, ⁷⁷Se, ⁹³Nb, ⁹⁵Mo, ¹⁰⁷Ag, ¹¹¹Cd, ¹¹⁵In, ¹¹⁸Sn, ¹²¹Sb, ¹²⁵Te, ¹³⁹La, ¹⁴⁰Ce, ¹⁴⁶Nd, ¹⁴⁷Sm, ¹⁵⁷Gd, ¹⁸²W, ¹⁸⁵Re, ¹⁹⁷Au, ²⁰²Hg, ²⁰⁵Tl, ²⁰⁸Pb, ²⁰⁹Bi, ²³²Th, and ²³⁸U. The targeted areas in the polished sections were predefined to try and avoid mineral inclusions. Repeated external standardization was conducted by analyzing NIST SRM 610 glass standard, and the USGS Mass 1 sulfide standard.

Data reduction was performed by using the Sb contents of stibnite measured by SEM-EDS as internal standards and the SILLS software [46]. During data reduction, peak-shaped fluctuations of the intensity signal of some isotopes were investigated in order to exclude the influence of other minerals on the chemical composition of the studied minerals. The full list of the LA-ICP-MS data, including elements ascribed to nano-scale mineral inclusions, is included in Table S3.

For the statistical analysis of the bulk geochemistry and the LA-ICP-MS analytical results, univariate analysis (minimum, maximum, standard deviation, and average), and bivariate analysis (Pearson's correlations: Table S4) were obtained. The SPSS (version 25.0.0) statistics software (IBM, New York, NY, USA) was used for the statistical analyses. Statistical graphs and time-resolved analytical profiles of LA-ICP-MS analyses were plotted using Grapher (version 16.1.335) software (Golden Software LLC, Golden, CO, USA).

3.6. Fluid Inclusion Micro-Thermometry

Seven doubly-polished wafers of quartz in the veins from the Gerakario porphyry and epithermal mineralization, were prepared at the University of Hamburg, Germany, and

were studied for fluid inclusions. A LINKAM THM-600/TMS 90 heating-freezing stage (Linkam, Surrey, UK) coupled to a Leitz SM-LUX-POL microscope (Leica Microsystems, Wetzlar, Germany) was used for the microthermometric measurements at the Department of Mineralogy-Petrology-Economic Geology, AUTh. Ice (H₂O) and organic reference substances with known melting points were used to calibrate the stage. The upper limit of heating was at 600 °C, with a precision of the measurements ± 1 °C during heating and ± 0.2 °C during freezing. The software packages FLUIDS [47] and SoWat [48] were used for the estimation of the fluid compositions and properties. Densities were calculated from equations proposed by Driesner [49].

4. Results

4.1. Bulk Geochemistry of Critical and Rare Metals in the Epithermal Quartz-Stibnite Veins

Two bulk samples (Ger 3.1, Ger 5) from the quartz-stibnite vein mineralization were geochemically analyzed. The critical and rare metal concentrations are given in the Table 1 (full geochemical dataset: Table S4). The quartz-stibnite veins are more enriched in Ag, Au, Bi, Cd, and Sb compared to those in the upper continental crust (UCC [50]) (Figure 4). In contrast, they are depleted in Ce, Co, Ga, La, and U (Figure 4). The trace elements Gd, Ge, Hg, In, Nb, Nd, Re, Se, Sm, Ta, Te, Th, Ti, V, and W exhibit concentrations below detection limits (Table 1, Figure 4). Antimony is the most enriched element reaching 574,000 ppm (57.4 wt.%), followed by Co (<1.8 ppm), Ag (<1.2 ppm), Ga (<0.16 ppm), Au (<0.05 ppm), Cd (<0.05 ppm), and Bi (<0.03 ppm) (Table 1). The concentrations of Ce and La reach 0.12 ppm and 0.4 ppm, respectively (Table 1).

4.2. Mode of Occurrence of Stibnite

Stibnite in the epithermal veins is massive and forms granular aggregates (Figure 3b). In some cases, stibnite inclusions (<100 μm in size) are found in quartz. Berthierite is commonly found as small inclusions in stibnite (Figure 5a) and locally as thin lamellae (Figure 3d). Euhedral pyrite (<50 μm in size) and arsenopyrite (<200 μm in size) (Figure 3c,d and Figure 5b,c), and ovoid inclusions of native antimony (<200 μm in size) (Figure 5a,d), occur scattered in stibnite. The oxidation of stibnite resulted in the formation of valentinite (<400 μm in size), near the walls of the veins (Figure 5b).

Table 1. Bulk geochemical analyses of selected critical and rare metals from the quartz-stibnite veins at Gerakario. The average values are also given. For the full list of geochemical analyses, see Table S4.

Host Rock		Two-Mica Gneiss			Host Rock		Two-Mica Gneiss		
Alteration		Sericitic Alteration			Alteration		Sericitic Alteration		
Element	Detection Limit	Ger 3.1	Ger 5	AVG	Element	Detection Limit	Ger 3.1	Ger 5	AVG
		ppm					ppm		
Ag	0.01	0.98	1.2	1.1	Nd	0.1	b.d.l.	b.d.l.	n.a.
Au	5×10^{-6}	0.05	0.04	0.05	Re	0.001	b.d.l.	b.d.l.	n.a.
Bi	0.01	0.02	0.03	0.03	Sb	0.01	326,000	574,000	450,000
Cd	0.01	0.05	0.04	0.05	Se	0.2	b.d.l.	b.d.l.	n.a.
Ce	0.02	0.09	0.12	0.11	Sm	0.03	b.d.l.	b.d.l.	n.a.
Co	0.1	1.8	0.9	1.4	Ta	0.01	b.d.l.	b.d.l.	n.a.
Ga	0.05	0.16	0.07	0.12	Te	0.01	b.d.l.	b.d.l.	n.a.
Gd	0.05	b.d.l.	b.d.l.	n.a.	Th	0.2	b.d.l.	b.d.l.	n.a.
Ge	0.05	b.d.l.	b.d.l.	n.a.	Tl	0.02	0.81	0.86	0.84
Hg	0.005	b.d.l.	b.d.l.	n.a.	Ti	50	b.d.l.	b.d.l.	n.a.
In	0.005	b.d.l.	b.d.l.	n.a.	U	0.05	0.09	0.13	0.11
La	0.2	0.4	0.4	0.4	V	1	b.d.l.	b.d.l.	n.a.
Nb	0.05	b.d.l.	b.d.l.	n.a.	W	0.05	b.d.l.	b.d.l.	n.a.

Abbreviation: AVG = average, b.d.l. = below detection limit.

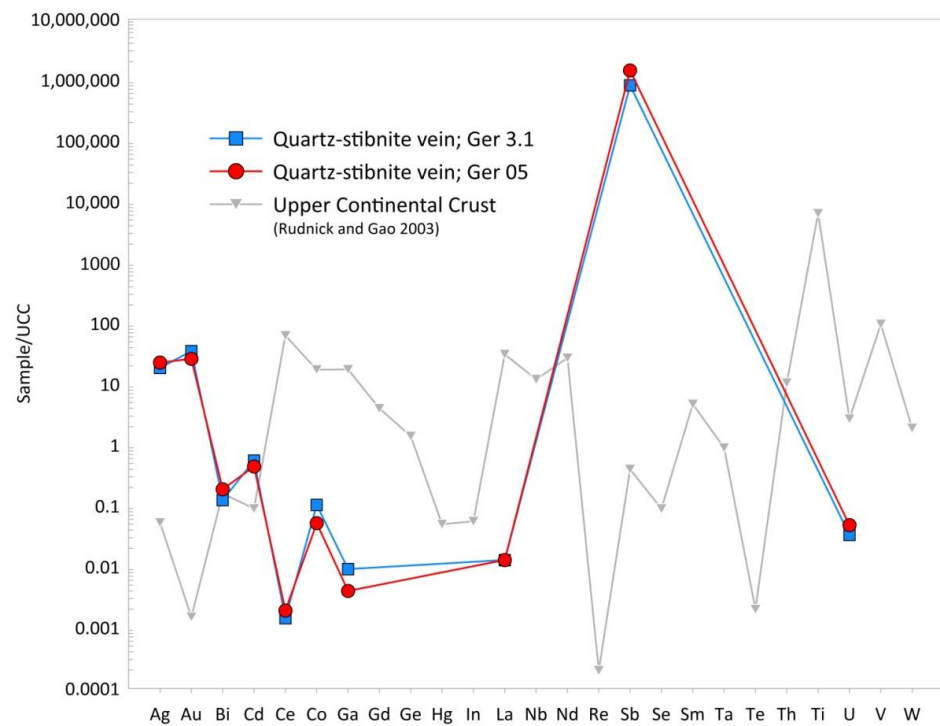


Figure 4. Upper continental crust (UCC) normalized logarithmic spider diagram of the two analyzed samples from the epithermal quartz-stibnite veins at Gerakario (UCC normalized values after Rudnick and Gao [50]).

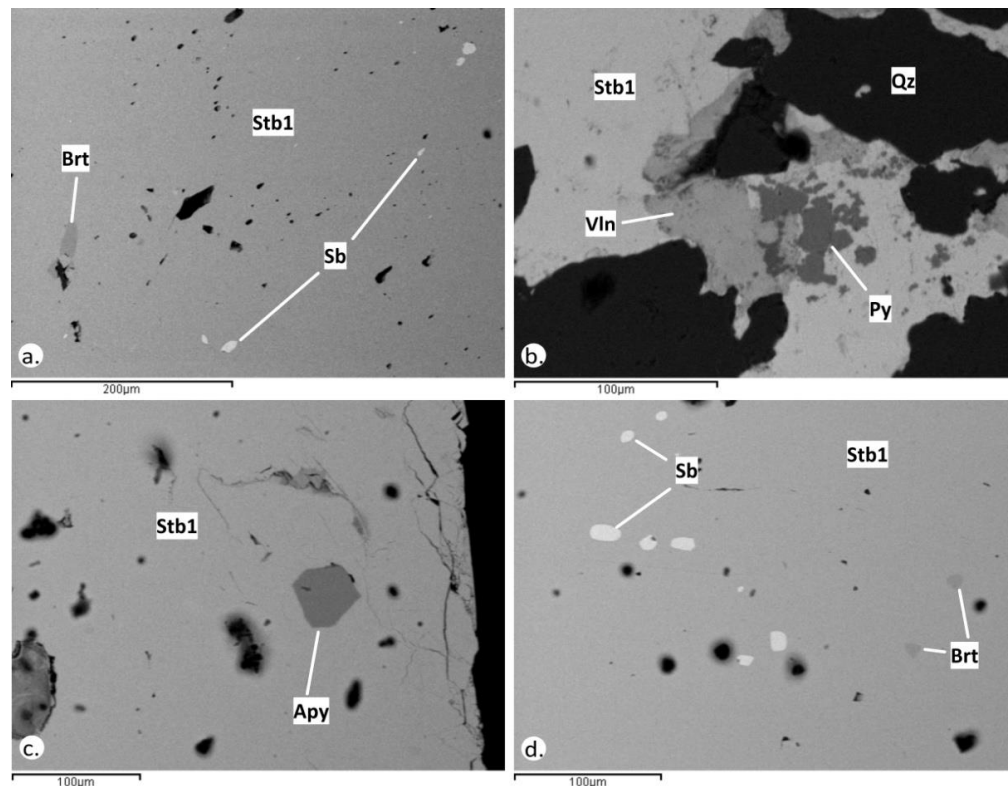


Figure 5. SEM back-scattered electron images of stibnite from the epithermal veins at Gerakario. (a) Massive stibnite (Stb1) and inclusions of berthierite (Brt) and native antimony (Sb). (b) Stibnite (Stb1) replaced by valentinite (Vln), and euhedral pyrite (Py) in quartz (Qz). (c) Euhedral arsenopyrite (Apy) in massive stibnite (Stb1). (d) Round-shaped inclusions of native antimony (Sb) and berthierite (Brt) in stibnite (Stb1).

4.3. Mineral Chemistry of Stibnite

Stibnite exhibits weak to moderate trace elemental contents (Table 2, Figure 6). The full analytical dataset is given in Supplementary Materials (Table S2). Base (As, Cu, Pb) and critical and rare metals (Ag, Bi, Ce, La, Re, Sm, Th, Ti, Tl) are incorporated in stibnite (Table 2). Lanthanum (<86 ppm) is the most common critical metal, followed by Ti (<18 ppm), Ag (<0.91 ppm), Tl (<0.56 ppm), Bi (<0.33 ppm), Ce (<0.32 ppm), Sm (<0.10 ppm), and Re (<0.03 ppm) (Table 2; Figure 6). The examination of ablation patterns reveals that critical and rare metals are incorporated in the stibnite lattice and that nano-scale mineral inclusions are not present.

4.4. Statistical Analysis of Trace Elements Concentrations in Stibnite

Pearson product-moment correlation coefficients for stibnite are described by significant positive correlation ($p < 0.01$; value = 0.919) defined for the elemental pair Ce-La, and by positive correlations ($p < 0.05$; values: 0.563–0.589) for the pairs Ce-Sb and La-Sb (Table S3). A negative correlation ($p < 0.05$; value: -0.564) was defined for the elemental pair Bi-Sb (Table S3).

4.5. Fluid Inclusions Petrography

A study of fluid inclusions from the Gerakario porphyry system by Tombouloglou [44] revealed that the potassic alteration and the Cu precipitation took place from an initial magmatic fluid with high homogenization temperatures ($T_h = 350\text{--}600\text{ }^\circ\text{C}$) and high salinities (45–70% wt.% NaCl equiv.). The subsequent sericitic alteration and sulfide mineralization were formed by boiling fluids with lower salinities (38–45% wt.% NaCl equiv.) at lower temperatures (350–400 °C). Inclusions along healed cracks with homogenization temperatures <350 °C were characterized as secondary [44].

To further constrain the character of the ore fluids and the formation conditions of the Gerakario deposit, a fluid inclusion study was conducted on quartz from A-type veins related to the potassic alteration of the porphyry mineralization, and from the epithermal stibnite-quartz veins. Quartz in the veins is semi-transparent and anhedral, with the grains forming triple junctions at angles of $\sim 120^\circ$ (Figure 7a), implying extensive recrystallization [51]. This is typical of early high temperature quartz veins in many porphyry copper systems and suggests that the fluid inclusions migrated to grain boundaries [52]. The continuous and multiple flows of fluids caused re-opening of the veins and dynamic recrystallization of the quartz and commonly destroy a large part of the fluid inclusion assemblages [51,52].

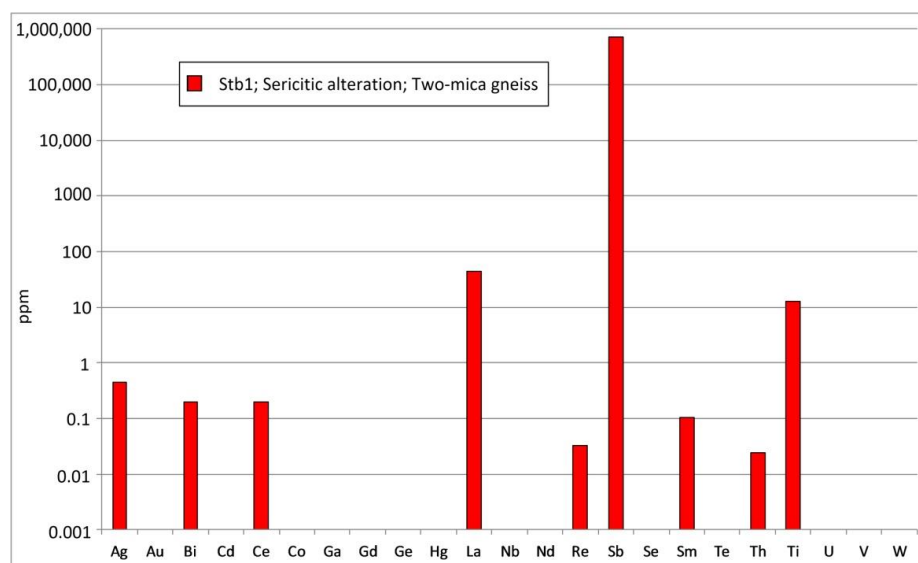


Figure 6. Average values of critical and rare metals concentrations of stibnite from the epithermal quartz-stibnite veins. Local enrichments related to nano-scale mineral inclusions are excluded.

Table 2. LA-ICP-MS analyses of stibnite from the quartz-stibnite veins at Gerakario (the full dataset in Table S2).

Alteration	Sericitic				Alteration	Sericitic			
Host Rock	Two-Mica Gneiss				Host Rock	Two-Mica Gneiss			
Mineralization Stage	Stb1; Epithermal Quartz-Stibnite Veins (<i>n</i> = 15)				Mineralization Stage	Stb1; Epithermal Quartz-Stibnite Veins (<i>n</i> = 15)			
Element/AVG. Detection Limit	MIN	MAX	STDEV	AVG	Element/AVG. Detection Limit	MIN	MAX	STDEV	AVG
ppm	ppm				ppm	ppm			
Ag/0.3	0.12	0.91	0.27	0.45	Nb/0.08	b.d.l.	b.d.l.	n.a.	n.a.
As/n.a.	12	231	70	62	Nd/0.56	b.d.l.	b.d.l.	n.a.	n.a.
Au/0.24	b.d.l.	b.d.l.	n.a.	n.a.	Pb/n.a.	98	165	23	122
Bi/0.24	0.15	0.33	0.05	0.2	Re/0.06	0.03	0.03	n.a.	0.03
Cd/0.9	b.d.l.	b.d.l.	n.a.	n.a.	Sb/n.a.	710,800	716,500	1.611	711,827
Ce/n.a.	0.09	0.32	0.08	0.2	Se/5.8	b.d.l.	b.d.l.	n.a.	n.a.
Co/0.25	b.d.l.	b.d.l.	n.a.	n.a.	Sm/0.33	0.10	0.10	n.a.	0.10
Cu/n.a.	29	55	8.6	40	Te/1.6	b.d.l.	b.d.l.	n.a.	n.a.
Ga/0.85	b.d.l.	b.d.l.	n.a.	n.a.	Th/0.06	0.02	0.02	n.a.	0.02
Gd/0.33	b.d.l.	b.d.l.	n.a.	n.a.	Ti/n.a.	9.7	18	2.3	13
Ge/2.5	b.d.l.	b.d.l.	n.a.	n.a.	Tl/0.32	0.35	0.56	0.11	0.48
Hg/0.27	b.d.l.	b.d.l.	n.a.	n.a.	U/0.04	b.d.l.	b.d.l.	n.a.	n.a.
In/0.06	b.d.l.	b.d.l.	n.a.	n.a.	V/0.52	b.d.l.	b.d.l.	n.a.	n.a.
La/n.a.	24	86	28	44	W/0.33	b.d.l.	b.d.l.	n.a.	n.a.

Abbreviations: AVG = average value, AVG. Detection Limit = Average detection limit, b.d.l. = below detection limit, MIN = minimum value, MAX = maximum value, *n* = number of analyses, n.a. = not applicable, STDEV = standard deviation.

In the present study, most of the fluid inclusions are arranged in clusters (Figure 7a–c) that have escaped recrystallization. These inclusions are characterized by similar shapes and sizes and constant liquid to vapor ratios, and consequently are classified as primary, on the basis of the criteria proposed by Roedder [53] and Goldstein and Reynolds [54]. Fluid inclusions distributed along the growth zones of quartz are extremely rare and too small for microthermometry. The maximum length of the primary inclusions reaches 32 μm . In addition to primary fluid inclusions, rare secondary inclusions occur along healed cracks. In several inclusions, post-entrapment phenomena (necking down or leaking) are common, and no measurements were performed on them.

Based on the phase ratios observed on the inclusions from the Gerakario porphyry system and the epithermal stibnite veins at room temperature, in combination with their behavior during heating and freezing, three types of primary fluid inclusions were identified.

Type 1 inclusions consist of two-phases a liquid aqueous phase and a vapor phase where the vapor bubble occupies 30–40% of the volume of the inclusion. These inclusions homogenize into the liquid phase and are found in the porphyry- and the epidermal-related veins (Figure 7b,c).

Type 2 inclusions comprise three or four phases (Figure 7b,d,e), one liquid, one vapor (occupying 30 to 40% of the volume of the inclusions), and one or rarely two solid phases halite and sylvite. In exceptional cases, another solid unidentified phase was observed (Figure 7d). Type 2 inclusions homogenize into the liquid phase by bubble disappearance.

Type 3 fluid inclusions are two phases, liquid-vapor inclusions where the latter occupies 80–90% of the volume of the inclusion (Figure 7f). These inclusions homogenize into the vapor phase and rarely contain one or two opaque minerals, which are likely hematite and chalcocopyrite (Figure 7e). Fluid inclusions of type 2 and 3 are found only in the porphyry system.

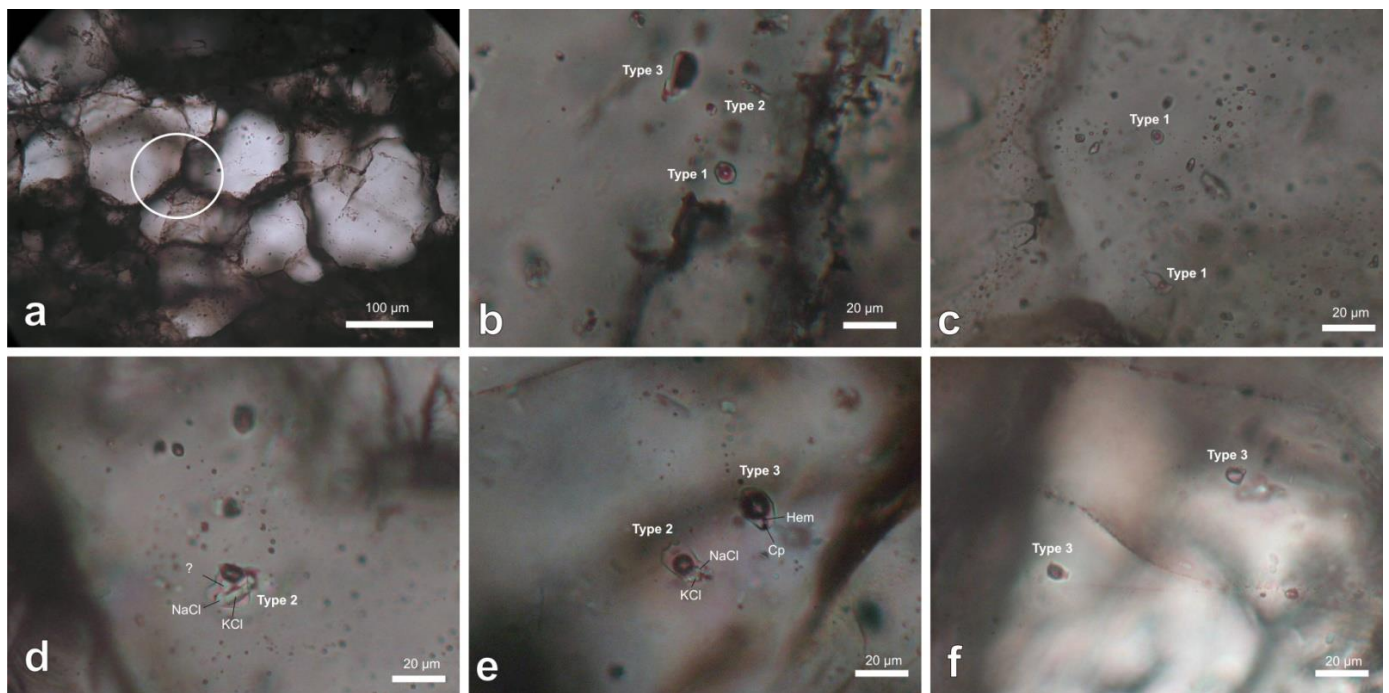


Figure 7. Clusters of fluid inclusions in quartz from the Gerakario porphyry and epithermal deposits. (a) Recrystallized quartz grains forming triple junctions with angles at 120° (white circle) in A-type porphyry vein. (b) Fluid inclusions of types 1, 2, and 3, in A-type porphyry vein. (c) Liquid-rich inclusions of type 1 in an epithermal stibnite vein. (d) Fluid inclusions of type 2 with three solid phases: halite (NaCl), sylvite (KCl), and an unidentified phase, possibly a Ca- or Mg-chloride, A-type porphyry vein. (e) Types 2 and 3 fluid inclusions in the porphyry system. Two solid phases, halite (NaCl and sylvite (KCl) are observed in the type 2 inclusion, whereas the type 3 inclusions contain two opaque phases, hematite (Hem and chalcopyrite (Cp)). (f) Vapor-rich type 3 inclusions in the porphyry system.

4.6. Microthermometry

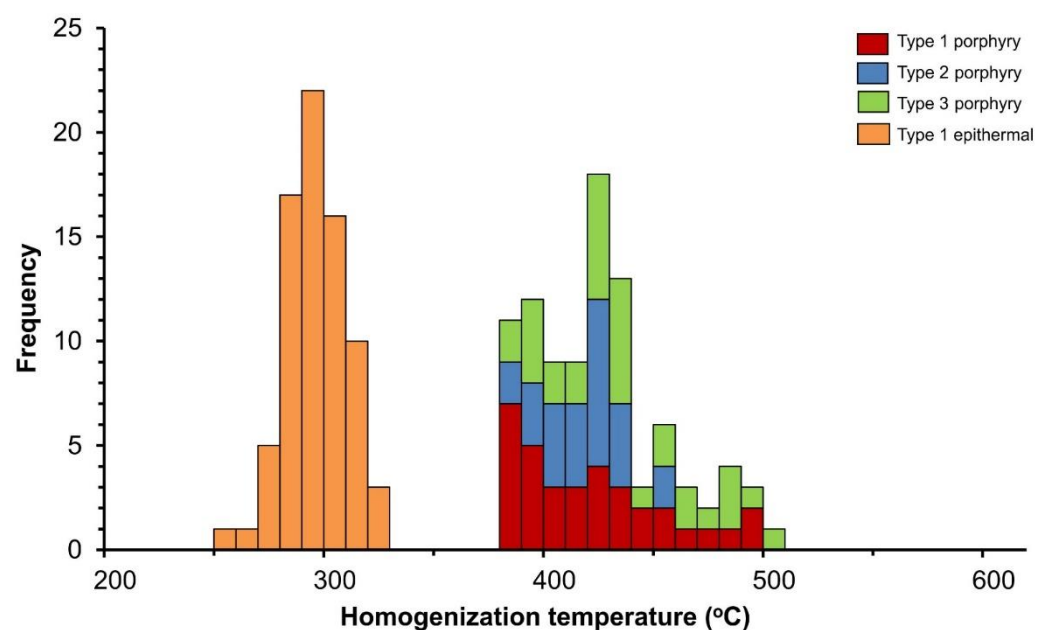
Initial melting temperatures of ice (T_e) of fluid inclusions from porphyry type mineralization, range from -33.0 to -46.4 °C. This indicates that, in addition to NaCl, other salts, such as KCl, $MgCl_2$, and/or $CaCl_2$, are dissolved in the fluid [55]. The final ice melting temperatures (T_m) of the Type 1 inclusions range between -19.4 and -10.8 °C, indicating a moderate to relatively high salinity of 14.8 to 22 wt.% NaCl equiv. [56]. In type 3 fluid inclusions, T_m range from -16.5 to -12 °C demonstrating moderate to relatively high salinities of 14.4 to 19.8 wt.% NaCl equiv. in the H_2O -NaCl-KCl system.

Type 1 inclusions homogenize (T_h) from 382° to 496 °C (Figure 8, Table 3), while type 2 inclusions homogenize with the disappearance of the vapor bubble after the disappearance of the solid phases (more commonly halite than sylvite). In rare cases, another unidentified solid phase was observed, which is probably a chloride complex of Mg or Ca. Homogenization temperatures in the Type 2 inclusions range from 381° to 458 °C (Figure 8, Table 3). Based on the solid phase homogenization temperatures (271 – 386 °C) and using the data for the system H_2O -NaCl [56], the salinity of the type 2 inclusions range from 35.7 to 45.6 wt.% NaCl equiv. Type 3 fluid inclusions homogenize at temperatures from 381° to 504 °C (Figure 8). Homogenization temperatures of the fluid inclusions of 1, 2, and 3 types in the porphyry style mineralization overlap between 380° and 460 °C, with a distinct maximum at ~ 430 °C (Figure 8).

Table 3. Microthermometric data from the different types of fluid inclusions in the porphyry and epithermal systems at Gerakario.

Mineralization Style	FI Type	Th (°C)	Tm (Ice) (°C)	Salinity (wt.% NaCl equiv.)
Porphyry style quartz veins (A-type)	1 L + V → L	382 to 496 (<i>n</i> = 34)	−19.4 to −10.8 (<i>n</i> = 6)	14.8 to 22.0
	2 L + V + S → L	381 to 458 (<i>n</i> = 27)	271 to 386 (<i>n</i> = 27)	35.7 to 45.6
	3 L + V → V	382 to 504 (<i>n</i> = 33)	−16.5 to −11.9 (<i>n</i> = 6)	14.4 to 19.8
Epithermal style quartz-stibnite veins	1 L + V → L	256 to 326 (<i>n</i> = 75)	−6.9 to −5.0 (<i>n</i> = 12)	7.9 to 10.4

Abbreviations: FI = Fluid inclusions; L = liquid aqueous phase; V = vapor phase; S = solid phase (halite, sylvite); Th = homogenization temperature; Tm (ice) = final ice melting temperature; *n* = number of microthermometric analyses.

**Figure 8.** Histogram showing the homogenization temperatures of the fluid inclusions from the porphyry (Types 1, 2, and 3) and the epidermal system (Type 1) at Gerakario.

High-salinity fluid inclusions (type 2) usually coexist with vapor-rich inclusions (type 3) within the same assemblage, demonstrating similar homogenization temperatures (Figures 7b,d and 8). This indicates a simultaneous heterogeneous trapping of two fluids, a saline brine (36–46 wt.% NaCl equiv.) and a low-density vapor-rich fluid with lower salinity (14–22 wt.% NaCl equiv.), which suggests fluids were trapped during boiling [53,56,57]. Fluids along the boiling curve do not require pressure correction; therefore, the homogenization temperatures represent the actual trapping temperatures of the fluid [57].

The initial melting temperatures of ice in the fluid inclusions of the quartz-stibnite epithermal veins vary between −38.7 and −49.9 °C. This indicates that, in addition to NaCl, other salts, such as KCl, MgCl₂, and/or CaCl₂, were involved in the ore-forming fluid [55]. The final ice melting temperatures of the type 1 inclusions range from −6.9 to −5.0 °C indicating relatively low salinities (7.9 to 10.4 wt.% NaCl equiv.) [56]. Homogenization temperatures vary from 256° to 326 °C, with a maximum at 290 °C (Figure 8).

5. Discussion

5.1. Conditions of Formation of the Porphyry Cu-Au Deposit at Gerakario

The porphyry Cu-Au deposit and the epithermal quartz-stibnite veins at Gerakario are related to the emplacement of a syenite intrusion in two-mica gneiss of the Vertiskos unit during the Miocene (22 ± 0.8 Ma; U-Pb zircon ages [42]), in an extensional structural

regime. The mineralization shares many similarities in its geotectonic setting, structural control, magma evolution, hydrothermal alteration, and physicochemical parameters of the hydrothermal fluids with the adjacent Vathi porphyry-epithermal system, which is genetically related to a quartz monzonite [32,33].

At Gerakario, the fast ascension of the syenite magma and its crystallization at shallow depths caused exsolution of hydrous fluids and silicate melts that resulted in hydraulic fracturing, increasing the permeability of the host rocks. This mechanism favored the formation of the potassic hydrothermal alteration and the deposition of the Cu-Au mineralization in the A-type veins, along fractures, under boiling conditions. Phase separation was favored by a rapid drop in temperature and pressure in the veins, resulting in a saline brine (36–46 wt.% NaCl equiv.) and a co-existing lower salinity (14–22 wt.% NaCl equiv.) low-density vapor-rich fluid that homogenize over the same temperature range, between 380° and 460 °C (Figure 9).

According to Brathwaite et al. [58], aqueous fluid inclusions with moderate salinity (up to 20 wt.% NaCl equiv.) represent a fluid extracted from the magma. In this case, the fluid is cooled to conditions between plastic and brittle deformation, creating inclusions enriched in the liquid (Type 1) and vapor phases (Type 3) at Gerakario, with moderate salinity, without forming liquid inclusions with halite [58].

The densities of the hydrothermal fluids at the Gerakario porphyry deposit are $>0.90 \text{ g.cm}^{-3}$ for the fluids with high salinity (type 2 fluid inclusions) and $<0.78 \text{ g.cm}^{-3}$ for the moderate salinity fluids (type 1 and 3 fluid inclusions). The trapping pressures of the fluid inclusions can be estimated considering that the fluids were trapped under boiling conditions in the system NaCl-KCl-CaCl₂-H₂O. Based on homogenization temperatures and the equation of Archer [59], the minimum trapping pressures for type 2 inclusions in A-type quartz veins range from 100 to 350 bar, and for type 3 inclusions from 240 to 580 bar. These pressures indicate a maximum ore formation depth of ~2 km under lithostatic conditions.

5.2. Genesis and Geochemistry of the Epithermal Quartz-Stibnite Veins at Gerakario

The epithermal veins formed from a fluid of low to moderate salinity (7.9 to 10.4 wt.% NaCl equiv.) with homogenization temperatures ranging mainly from 280° to 320 °C, with a maximum at 290 °C (Figure 9). This fluid resulted from the mixing of a high to moderate salinity fluid exsolved from the porphyry system, and meteoric water, at the final stage of the magmatic-hydrothermal system in an epithermal environment. Due to the shallow depth of formation of these veins, the pressure correction should be $<10 \text{ °C}$ (e.g., Bodnar et al. [60]). For this reason, the homogenization temperatures (280–320 °C, with a maximum of 290 °C) correspond to the minimum temperatures of the formation of the epidermal veins. Therefore, for hydrostatic pressures in the range of 65 to 116 bar, a depth of 600 to 1000 m under hydrostatic conditions is proposed for the stibnite mineralization.

The local structural setting (NE-SW and E-W trending normal to oblique faults) enhanced hydrothermal fluid circulation and mixing with meteoric water. As a result, base metal mineralization formed in the surrounding metamorphic rocks [39] (Figure 2). The epithermal quartz-stibnite veins are hosted in the sericitically altered gneiss. They are mostly continuous, and consist of stibnite + berthierite + native antimony + pyrite + arsenopyrite ± (marcasite, pyrrhotite, chalcopyrite, löllingite, native gold) [39,45] (Figures 3a–d and 5a–d).

Bulk geochemical analysis revealed enrichment in Co ($<1.8 \text{ ppm}$), Ag ($<1.2 \text{ ppm}$), Ga ($<0.16 \text{ ppm}$), Ce ($<0.12 \text{ ppm}$), La ($<0.4 \text{ ppm}$), Au ($<0.05 \text{ ppm}$), Cd ($<0.05 \text{ ppm}$), and Bi ($<0.03 \text{ ppm}$) (Table 1). The depletion in Hg is profound (Table 1) and is in contrast to the Hg enriched character of the Sb ores located in SE China, where the formation of the epithermal deposits is ascribed to mineralizing fluids enriched in Sb-As-Hg-(Au-Tl-U) [16,21]. Noteworthy are the relatively elevated concentrations of Ce ($<0.32 \text{ ppm}$) and La ($<86 \text{ ppm}$), as REEs are not commonly incorporated in epithermal systems [10].

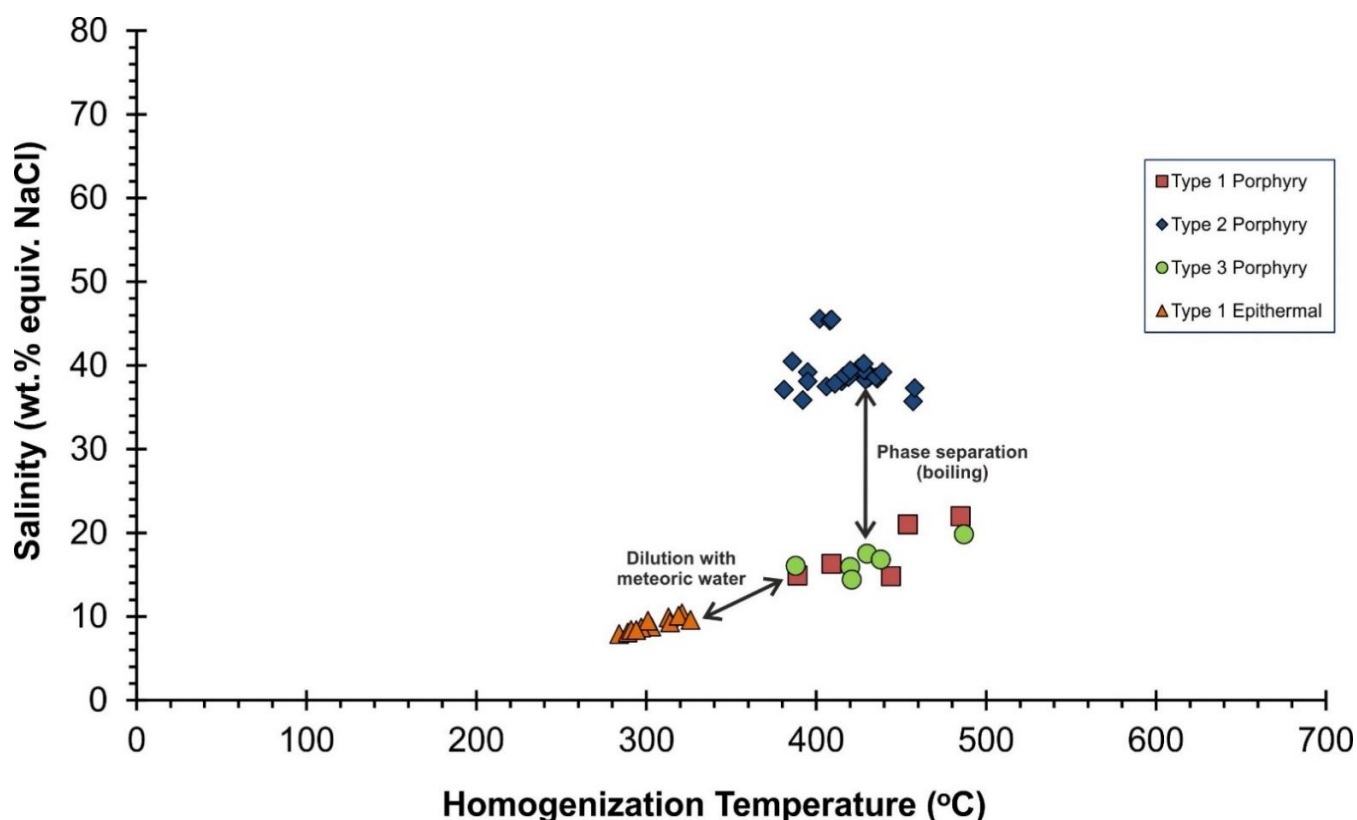


Figure 9. Diagram of salinity versus homogenization temperature of the fluid inclusions in the porphyry-epithermal system at Gerakario.

Hydrothermal carbonates (e.g., calcite) mainly host REEs in the epithermal systems [21]. In these cases, REE fractionation is dependent upon the composition of the mineralizing fluids and the co-precipitating of other ore, gangue, and alteration minerals [21]. During precipitation of calcite, medium and heavy REEs are preferentially incorporated in its crystal lattice, while light REEs, especially La, are enriched in the residual fluid [21]. Thus, significant contents of La and Ce, and rarely Pr, Nd, and Sm are incorporated in stibnite, which formed after calcite [21]. Leaching of carbonate wall rocks and of rock-forming minerals from the magmatic fluids may introduce REEs to the circulating hydrothermal system [21]. A similar mechanism has been proposed for the REE enrichment detected in the oxidation zone of the adjacent Vathi porphyry Cu-Au \pm Mo deposit [32] (Figure 1).

In addition, REE incorporation in minerals is related to specific physicochemical factors, including the structure of the lattice and complexation (i.e., the combination of individual atom groups, ions or molecules to create one large ion or molecule [61]), as well as sorption and desorption [21]. Magmatic fluids are generally depleted in REEs, while meteoric fluids are slightly enriched in light REEs [62].

The anatomy of the quartz-stibnite veins at Gerakario, the ore assemblage, the bulk geochemistry, and the fluid inclusion study suggest that the ore mineralization was developed from intermediate to low sulfidation hydrothermal fluids, in a fault-induced epithermal stage set at the periphery of the Cu-Au porphyry system. The same could be suggested for all the base metals vein sets found in the vicinity of the Gerakario porphyry system. Epithermal, high to low sulfidation veins are commonly found peripheral to porphyry systems and porphyritic intrusions [19,63]. Epithermal veins are associated with several porphyry deposits in Greece (e.g., Pagoni Rachi, Maronia, Vathi) [24,33,64]. However, the veins in these deposits do not host massive stibnite [24]. Epithermal veins with massive stibnite and realgar are found distal to porphyritic intrusions located at Chios island and the

Agia area (Mavrovounio mountain). In those deposits, a zoning proximal to the intrusions containing Sn and Pb-Zn-Cu sulfides was identified by Voudouris et al. [24].

5.3. Mineral Chemistry of Stibnite and Nano-Scale Inclusions

The trace elemental study of stibnite by means of LA-ICP-MS needs further development [16]. To our knowledge, this study presents for the first time the mineral chemistry of stibnite from epithermal veins found in the periphery of a porphyry system [16]. Stibnite (Stb1) at Gerakario is enriched in base metals (As, Cu, Pb) and bears weak to moderate contents of critical and rare metals (Ag, Bi, Ce, La, Re, Sm, Th, Ti, Tl) (Table 2, Figure 6). However, it is depleted in Au, Hg, Se, and Te with concentrations below detection limits (Table 2). The depletion of Hg in stibnite contrasts to the Hg enrichment in stibnite from SE China [16]. In addition, the depletion of Au^{+1} as solid solutions in stibnite and the presence of native gold in interstices of the quartz-stibnite veins [45] indicate that Au precipitation slightly followed Sb precipitation. Thus, it could be suggested that the precipitation of massive stibnite depleted the H_2S content of the mineralizing fluids, and enhanced the precipitation of native gold (Au^0) in the quartz-epithermal veins [65].

The concentrations of As, Cu, and Pb in stibnite can be attributed to the stoichiometric substitutions of Sb ($2\text{Sb}^{3+} \leftrightarrow \text{Cu}^{++}\text{Pb}^{2++}\text{As}^{3+}$), as well as, in some cases, to invisible nanoparticles or to higher incorporation of an element in a specific sector zone, as the LA-ICP-MS depth profiles locally consist of a series of peaks of slightly varying size (Figure 10a,b) [16]. In addition, Cu and Pb exhibit a more consistent distribution in stibnite relatively to the As distribution (Table 2).

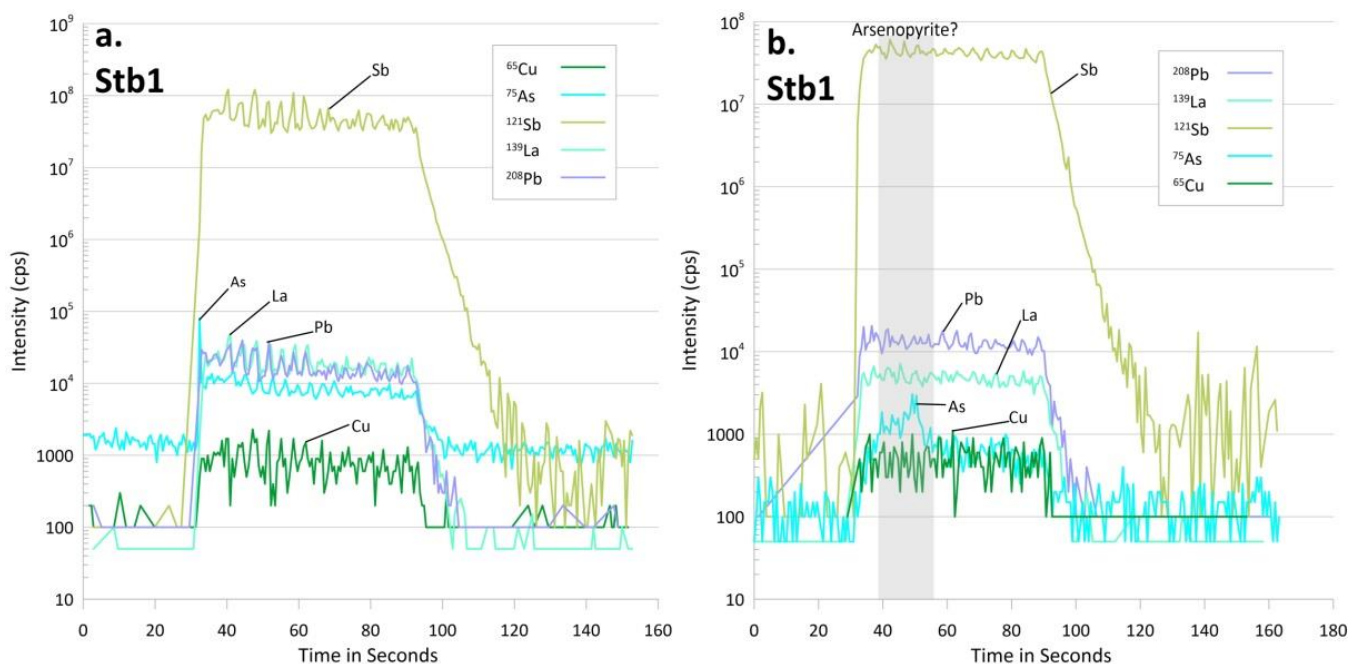


Figure 10. Selected time-resolved laser ablation ICP-MS depth profiles of stibnite from the epithermal quartz-stibnite veins at Gerakario. (a) In Stb1, the distribution patterns of As, La, Pb, Cu, and Sb are similar, suggesting their affiliation with stibnite. (b) In Stb1, the spiky pattern for As shows the presence of nano-scale inclusions of arsenopyrite in stibnite or that As is incorporated in higher amounts in a specific stibnite sector zone.

The depth profile of La exhibits a similar pattern to those of Sb, As, Cu, and Pb (Figure 10a,b). The crystal lattice of stibnite does not include proper sites for REE accommodation, especially for La [21]. Thus, following the suggestions of Wang et al. [21], lanthanum in stibnite at Gerakario may occur in fluid inclusions or in lattice defects. The rest of the critical and rare metals, including Ag, Bi, Ce, Re, Th, Ti, and Tl, which are detected in stibnite, display depth profiles close to background values. Regarding Ce and

La contents, possible matrix-derived interferences (i.e., $^{121}\text{Sb}^{18}\text{O}(\pm\text{H})$ for La and Ce) could not be excluded and the distribution of these elements needs further investigation.

The depletion of stibnite in Hg, Se, and Te, and the enrichment in La could suggest that it was deposited during the late stages of the mineralizing events in the porphyry-epithermal system at Gerakario. In addition, the other Fe-Cu-Pb-As vein mineralization found in the periphery of the porphyry system [39] (Figure 2), and the enrichment of As, Cu, and Pb in stibnite, indicate the predominance of base metals in the mineralizing fluids related to the epithermal stage.

6. Conclusions

The epithermal quartz-stibnite veins of Gerakario are genetically related to a Cu-Au porphyry deposit hosted mainly in a syenite intrusion of Miocene age. Disseminated pyrite and chalcopyrite, and stockworks of A-type veins containing magnetite-pyrite-chalcopyrite, are found in the potassic alteration of the porphyry system. Minor pyrite and chalcopyrite occur as disseminations and in D-type veins in the sericitic alteration. The epithermal quartz veins include stibnite, berthierite, native antimony, pyrite, arsenopyrite, and traces of marcasite, pyrrhotite, chalcopyrite, löllingite, and native gold. Enrichment of these veins in critical and rare metals includes Ag, Au, Bi, Ce, Co, Ga, La, and Sb. The laser ablation ICP-MS analysis of stibnite show elevated concentrations of As, Cu, and Pb, and enrichments in Ag, Bi, Ce, La, Re, Sm, Th, Ti, and Tl. Correlation coefficients for the elemental pairs Ce-La, Ce-Sb, and La-Sb in stibnite indicate positive correlations, while the pair Bi-Sb shows a negative correlation. The formation of A-type veins in the potassic alteration of the porphyry system is ascribed to fluid boiling at temperatures between 380° and 460 °C at a depth <2 km. The epithermal quartz-stibnite veins were deposited under a lower temperature range (280–320 °C) at a depth between 600 and 1000 m.

Supplementary Materials: The following are available online at <https://www.mdpi.com/article/10.3390/app12020909/s1>, Table S1: Bulk geochemistry, Table S2: SEM-EDS data, Table S3: LA-ICP-MS data, Table S4: Pearson's correlation coefficient table.

Author Contributions: Conceptualization, C.L.S., V.M.; methodology, V.M., P.V., L.P., I.P.; formal analysis, L.P., E.S., D.D.; data curation, C.L.S., E.S., D.D.; writing—original draft preparation, C.L.S., V.M.; writing—review and editing, C.L.S., V.M., P.V., L.P., P.G.S., I.P., D.D., E.S.; supervision, V.M., P.V.; funding acquisition, C.L.S. All authors have read and agreed to the published version of the manuscript.

Funding: The ore microscopy and rock geochemistry investigation was funded by a research grant from the Society of Economic Geologists Canada Foundation (SEGCF) Fund. C.L.S. received a scholarship co-financed by Greece and the European Union (European Social Fund- ESF) through the Operational Program «Human Resources Development, Education and Lifelong Learning» in the context of the project “Strengthening Human Resources Research Potential via Doctorate Research—2nd Round” (MIS-5000432), implemented by the State Scholarships Foundation (IKY).

Institutional Review Board Statement: Not applicable.

Informed Consent Statement: Not applicable.

Data Availability Statement: Data is contained within the article.

Acknowledgments: The authors would like to acknowledge the Geological Institute of the Bulgarian Academy of Sciences for facilitating the LA-ICP-MS analysis. Katerina Giouri is especially thanked for her advices on statistical analysis. Two anonymous reviewers and the academic editors Adam Piestrzyński and Stanisław Z. Mikulski are especially thanked for their comments improving the quality of this article.

Conflicts of Interest: The authors declare no conflict of interest. The funders had no role in the design of the study; in the collection, analyses, or interpretation of data; in the writing of the manuscript, or in the decision to publish the results.

References

1. Humphreys, D. The mining industry and the supply of critical minerals. In *Critical Metals Handbook*; Gunn, G., Ed.; John Wiley & Sons: Hoboken, NJ, USA, 2014; pp. 20–40.
2. Huston, D.L. New age metals: The geology and genesis of ores required for a changing economy and a carbon-constrained world—preface to a thematic issue on critical commodities. *Miner. Depos.* **2014**, *49*, 885–887. [[CrossRef](#)]
3. European Commission. *Critical Raw Materials Resilience: Charting a Path towards Greater Security and Sustainability*; European Commission: Brussels, Belgium, 2020; p. 24.
4. Barakos, G.; Gutzmer, J.; Mischo, H. Strategic evaluations and mining process optimization towards a strong global REE supply chain. *J. Sustain. Min.* **2016**, *15*, 26–35. [[CrossRef](#)]
5. Dostal, J. Rare metal deposits associated with alkaline/peralkaline igneous rocks. In *Rare Earth and Critical Elements in Ore Deposits*; Verplanck, P.L., Hitzman, M.W., Eds.; Society of Economic Geologists Inc.: Littleton, CO, USA, 2016; pp. 33–54.
6. Sengupta, D.; Van Gosen, B.S. Placer-type rare earth element deposits. In *Rare Earth and Critical Elements in Ore Deposits*; Verplanck, P.L., Hitzman, M.W., Eds.; Society of Economic Geologists Inc.: Littleton, CO, USA, 2016; pp. 81–100.
7. Verplanck, P.L.; Mariano, A.N.; Mariano, A., Jr. Rare earth element ore geology of carbonatites. In *Rare Earth and Critical Elements in Ore Deposits*; Verplanck, P.L., Hitzman, M.W., Eds.; Society of Economic Geologists Inc.: Littleton, CO, USA, 2016; pp. 5–32.
8. John, D.A.; Taylor, R.D. By-products of porphyry copper and molybdenum deposits. In *Rare Earth and Critical Elements in Ore Deposits*; Verplanck, P.L., Hitzman, M.W., Eds.; Society of Economic Geologists Inc.: Littleton, CO, USA, 2016; pp. 137–164.
9. Velásquez, G.; Carrizo, D.; Salvi, S.; Vela, I.; Pablo, M.; Pérez, A. Tracking cobalt, REE and gold from a porphyry-type deposit by LA-ICP-MS: A geological approach towards metal-selective mining in tailings. *Minerals* **2020**, *10*, 109. [[CrossRef](#)]
10. Hofstra, A.H.; Kreiner, D.C. *Systems-Deposits-Commodities-Critical Minerals Table for the Earth Mapping Resources Initiative*; No. 2020-1042; U.S. Geological Survey: Reston, VA, USA, 2020; p. 24.
11. Goldfarb, R.J.; Hofstra, A.H.; Simmons, S.F. Critical elements in Carlin, epithermal, and orogenic gold deposits. In *Rare Earth and Critical Elements in Ore Deposits*; Verplanck, P.L., Hitzman, M.W., Eds.; Society of Economic Geologists Inc.: Littleton, CO, USA, 2016; pp. 217–244.
12. Deditius, A.P.; Utsunomiya, S.; Reich, M.; Kesler, S.E.; Ewing, R.C.; Hough, R.; Walshe, J. Trace metal nanoparticles in pyrite. *Ore Geol. Rev.* **2011**, *42*, 32–46. [[CrossRef](#)]
13. Cook, N.J.; Ciobanu, C.L.; Pring, A.; Skinner, W.; Shimizu, M.; Danyushevsky, L.; Saini-Eidukat, B.; Melcher, F. Trace and minor elements in sphalerite: A LA-ICPMS study. *Geochim. Cosmochim. Acta* **2009**, *73*, 4761–4791. [[CrossRef](#)]
14. George, L.L.; Cook, N.J.; Crowe, B.B.; Ciobanu, C.L. Trace elements in hydrothermal chalcopyrite. *Mineral. Mag.* **2018**, *82*, 59–88. [[CrossRef](#)]
15. George, L.L.; Cook, N.J.; Ciobanu, C.L. Minor and trace elements in natural tetrahedrite-tennantite: Effects on element partitioning among base metal sulphides. *Minerals* **2017**, *7*, 17. [[CrossRef](#)]
16. Fu, S.; Hu, R.; Bi, X.; Sullivan, N.A.; Yan, J. Trace element composition of stibnite: Substitution mechanism and implications for the genesis of Sb deposits in southern China. *Appl. Geochem.* **2020**, *118*, 104637. [[CrossRef](#)]
17. Dill, H.G.; Pertold, Z.; Kilibarda, R.C. Sediment-hosted and volcanic-hosted Sb vein mineralization in the Potosi region, Central Bolivia. *Econ. Geol.* **1997**, *92*, 623–632. [[CrossRef](#)]
18. Dill, H.G.; Melcher, F.; Botz, B. Meso- to epithermal W-bearing Sb vein-type deposits in calcareous rocks in western Thailand; with special reference to their metallogenetic position in SE Asia. *Ore Geol. Rev.* **2008**, *34*, 242–262. [[CrossRef](#)]
19. Wang, L.; Qin, K.Z.; Song, G.X.; Li, G.M. A review of intermediate sulfidation epithermal deposits and subclassification. *Ore Geol. Rev.* **2019**, *107*, 434–456. [[CrossRef](#)]
20. Cook, N.J.; Ciobanu, C.L.; Giles, D.; Wade, B. Correlating textures and trace elements in ore minerals. Mineral deposit research for a high-tech world. In Proceedings of the 12th Biennial SGA Meeting, Uppsala, Sweden, 12–15 August 2013; Jonsson, E., Ed.; Geological Survey of Sweden: Uppsala, Sweden, 2013; pp. 288–291.
21. Wang, J.; Wen, H.; Fan, H.; Zhu, J. Sm-Nd geochronology, REE geochemistry and C and O isotope characteristics of calcites and stibnites from the Banián antimony deposit, Guizhou Province, China. *Geochem. J.* **2012**, *46*, 393–407. [[CrossRef](#)]
22. Cassard, D.; Bertrand, G.; Billa, M.; Serrano, J.J.; Tourlière, B.; Angel, J.M.; Gaál, G. ProMine mineral databases: New tools to assess primary and secondary mineral resources in Europe. In *3D, 4D and Predictive Modelling of Major Mineral Belts in Europe*. *Mineral Resource Reviews*; Weihed, P., Ed.; Springer: Cham, Switzerland, 2015; pp. 9–58.
23. Melfos, V.; Voudouris, P. Cenozoic metallogeny of Greece and potential for precious, critical and rare metals exploration. *Ore Geol. Rev.* **2017**, *89*, 1030–1057. [[CrossRef](#)]
24. Voudouris, P.; Mavrogonatos, C.; Spry, P.G.; Baker, T.; Melfos, V.; Klemd, R.; Haase, K.; Repstock, A.; Djiba, A.; Bismayer, U.; et al. Porphyry and epithermal deposits in Greece: An overview, new discoveries, and mineralogical constraints on their genesis. *Ore Geol. Rev.* **2019**, *107*, 654–691. [[CrossRef](#)]
25. Arvanitidis, N.D. New metallogenetic concepts and sustainability perspectives for non-energy metallic minerals in Central Macedonia, Greece. *Bull. Geol. Soc. Greece* **2010**, *43*, 2437–2445. [[CrossRef](#)]
26. Tsirambides, A.; Filippidis, A. Metallic mineral resources of Greece. *Cent. Eur. J. Geosci.* **2012**, *4*, 641–650.
27. Tsirambides, A.; Filippidis, A. Gold metallogeny of the Serbomacedonian-Rhodope metallogenic belt (SRMB). *Bull. Geol. Soc. Greece* **2016**, *50*, 2037–2046. [[CrossRef](#)]

28. Tsirambides, A.; Filippidis, A. Sb- Bi-bearing metallogeny of the SerboMacedonian-Rhodope Metallogenic Belt (SRMB). *Bull. Geol. Soc. Greece* **2019**, *55*, 34–64. [[CrossRef](#)]
29. Melfos, V.; Voudouris, P.C. Geological, mineralogical and geochemical aspects for critical and rare metals in Greece. *Minerals* **2012**, *2*, 300–317. [[CrossRef](#)]
30. Baker, T. Gold \pm copper endowment and deposit diversity in the Western Tethyan magmatic belt, southeast Europe: Implications for exploration. *Econ. Geol.* **2019**, *114*, 1237–1250. [[CrossRef](#)]
31. Stergiou, C.L.; Melfos, V.; Voudouris, P. *A Review on the Critical and Rare Metals Distribution throughout the Vertiskos Unit, N. Greece*; MDPI: Basel, Switzerland, 2018.
32. Stergiou, C.L.; Melfos, V.; Voudouris, P.; Spry, P.G.; Papadopoulou, L.; Chatzipetros, A.; Giouri, K.; Mavrogonatos, C.; Filippidis, A. The geology, geochemistry, and origin of the porphyry Cu-Au-(Mo) system at Vathi, Serbo-Macedonian Massif, Greece. *Appl. Sci.* **2021**, *11*, 479. [[CrossRef](#)]
33. Stergiou, C.L.; Melfos, V.; Voudouris, P.; Papadopoulou, L.; Spry, P.G.; Peytcheva, I.; Dimitrova, D.; Stefanova, E.; Giouri, K. Rare and Critical Metals in Pyrite, Chalcopyrite, Magnetite, and Titanite from the Vathi Porphyry Cu-Au \pm Mo Deposit, Northern Greece. *Minerals* **2021**, *11*, 630. [[CrossRef](#)]
34. Vavelidis, M.; Melfos, V.; Kiliass, A. The gold-bearing quartz veins in the metamorphic rocks at the Drakontio area, central Macedonia, northern Greece. Mineral Deposits, Process to Processing. In Proceedings of the Fifth Biennial SGA Meeting and the Tenth Quadrennial IAGOD Symposium, London, UK, 22–25 August 1999; Stanley, C.J., Ed.; Balkema: Rotterdam, The Netherlands, 1999; Volume 1, pp. 209–212.
35. Bristol, S.K.; Spry, P.G.; Voudouris, P.C.; Melfos, V.; Mathur, R.D.; Fornadel, A.P.; Sakellaris, G.A. Geochemical and geochronological constraints on the formation of shear-zone hosted Cu-Au-Bi-Te mineralization in the Stanos area, Chalkidiki, northern Greece. *Ore Geol. Rev.* **2015**, *66*, 266–282. [[CrossRef](#)]
36. Skoupras, E. Study of the Stibnite Ore Mineralization in Rizana, Kilkis. Master's Thesis, Aristotle University of Thessaloniki, Thessaloniki, Greece, 2019.
37. Dimou, E. Native minerals in rocks and mineralizations of Greece and their significance. *Bull. Geol. Soc. Greece* **1989**, *23*, 207–223.
38. Vasilatos, C.; Mparlas, K.; Stamatakis, M.; Tsvivilis, S. Wolframite-stibnite mineral assemblages from Rizana Lachanas, Macedonia, Greece, and their possible use as flux agent in the manufacturing of clinker. *Bull. Geol. Soc. Greece* **2001**, *34*, 827–834. [[CrossRef](#)]
39. Toumanidou, O.C. Preliminary Study of the Porphyry System in Gerakario of Kilkis. Master's Thesis, Aristotle University of Thessaloniki, Thessaloniki, Greece, 2019.
40. Kelepertsis, A.E.; Reeves, R.; Andrulakis, J. Geochemical studies of porphyry type mineralization at Gerakario-Vathi of Kilkis area, northern Greece. *Miner. Wealth* **1986**, *42*, 43–48.
41. Miggiros, G.; Ioannidis, K.; Kelepertsis, A. *Geological Map of Greece: Herson Map Sheet, 1:50,000*; Hellenic Survey of Geology and Mineral Exploration (HSGME): Athens, Greece, 1990.
42. Frei, R. Isotope (Pb, Rb-Sr, S, O, C, U-Pb) Geochemical Investigations on Tertiary Intrusives and Related Mineralizations in the Serbomacedonian Pb-Zn, Sb + Cu-Mo Metallogenic Province in Northern Greece. Ph.D. Thesis, Swiss Federal Institute of Technology (ETH) Zurich, Zurich, Switzerland, 1992.
43. Tompouloglou, C. Les Minéralisations Tertiaires, Type Cuivre Porphyrique, du Massif Serbo-Macédonien (Macédoine, Grèce) Dans Leur Context Magmatique (Avec un Traitement Géostatistique pour les Données du Prospect d'Alexia). Ph.D. Thesis, Ecole Nationale Supérieure des Mines de Paris, Paris, France, 1981.
44. Tompouloglou, C. Etude d'inclusions fluides dans le context hydrothermal de mineralisations tertiaires, type cuivre porphyrique, du Massif Serbo-Mecadonien en Mecedoine, Grece. In *Special Volume in Honor of the Emeritus Professor Ioannis Papageorgakis*; Metsovion National Technical University: Athens, Greece, 2001; pp. 225–261.
45. Dimou, E.; Papastavrou, S.; Sermet, R. *Antimony in Greece, Samos Island, Gerakario Kilkis, Pefka Rhodope, Stagira Chalkidiki*; Hellenic Survey of Geology and Mineral Exploration (HSGME): Athens, Greece, 1987; Volume 3, p. 68.
46. Guillon, M.; Meier, D.L.; Allan, M.M.; Heinrich, C.A.; Yardley, B.W.D. SILLS: A MATLAB-based program for the reduction of laser ablation ICP-MS data of homogeneous materials and inclusions. In *Laser Ablation ICP-MS in the Earth Sciences: Current Practices and Outstanding Issues*; Sylvester, P., Ed.; Mineralogical Association of Canada Short Course 40: Vancouver, BC, Canada, 2008; pp. 328–333.
47. Bakker, R.J. Package FLUIDS. Part 4: Thermodynamic modelling and purely empirical equations for H₂O-NaCl-KCl solutions. *Mineral. Petrol.* **2012**, *105*, 1–29. [[CrossRef](#)]
48. Driesner, T.; Heinrich, C.A. The system H₂O-NaCl. Part I: Correlations for molar volume, enthalpy, and isobaric heat capacity from 0 to 1000 °C, 1 to 5000 bar, and 0 to 1 X-NaCl. *Geochim. Cosmochim. Acta* **2007**, *71*, 4880–4901. [[CrossRef](#)]
49. Driesner, T. The system H₂O-NaCl. Part II: Correlations for molar volume, enthalpy, and isobaric heat capacity from 0 to 1000 °C, 1 to 5000 bar, and 0 to 1 XNaCl. *Geochim. Cosmochim. Acta* **2007**, *71*, 4902–4919. [[CrossRef](#)]
50. Rudnick, R.L.; Gao, S. Composition of the continental crust. In *The Crust*, 1st ed.; Rudnick, R.L., Holland, H.D., Turekian, K.K., Eds.; Elsevier: Amsterdam, The Netherlands, 2005; pp. 1–64.
51. Monecke, T.; Monecke, J.; Reynolds, T.J.; Tsuruoka, S.; Bennett, M.M.; Skewes, W.B.; Palin, R.M. Quartz solubility in the H₂O-NaCl System: A framework for understanding vein formation in porphyry copper deposits. *Econ. Geol.* **2018**, *113*, 1007–1046. [[CrossRef](#)]
52. Tarantola, A.; Diamond, L.W.; Stünitz, H.; Thust, A.; Pec, M. Modification of fluid inclusions in quartz by deviatoric stress. III: Influence of principal stresses on inclusion density and orientation. *Contrib. Mineral. Petrol.* **2012**, *164*, 537–550. [[CrossRef](#)]

53. Roedder, E. Fluid inclusions. *Rev. Miner.* **1984**, *12*, 644.
54. Goldstein, R.H.; Reynolds, T.J. *Systematics of Fluid Inclusions in Diagenetic Minerals*; Society for Sedimentary Geology: Broken Arrow, OK, USA, 1994; p. 199.
55. Shepherd, T.; Rankin, A.; Alderton, D. *A Practical Guide to Fluid Inclusion Studies*, 1st ed.; Blackie and Son: Glasgow, UK, 1985; p. 239.
56. Bodnar, R.J. Introduction to fluid inclusions. In *Fluid Inclusions: Analysis and Interpretation*; Samson, I.M., Anderson, A.J., Marshall, D.D., Eds.; Society for Sedimentary Geology: Broken Arrow, OK, USA, 2003; Volume 32, pp. 1–8.
57. Audétat, A.; Pettke, T.; Heinrich, C.A.; Bodnar, R.J. Special paper: The composition of magmatic-hydrothermal fluids in barren and mineralized intrusions. *Econ. Geol.* **2008**, *103*, 877–908. [[CrossRef](#)]
58. Brathwaite, R.L.; Simpson, M.; Faure, K.; Skinner, D. Telescoped porphyry Cu-Mo-Au mineralisation, advanced argillic alteration and quartz-sulphide-gold-anhydrite veins in the Thames District, New Zealand. *Miner. Depos.* **2001**, *36*, 623–640. [[CrossRef](#)]
59. Archer, D.G. Thermodynamic properties of the NaCl + H₂O system. II. Thermodynamic properties of NaCl (aq), NaCl·2H₂ (cr), and phase equilibria. *J. Phys. Chem. Ref. Data* **1992**, *21*, 793–829. [[CrossRef](#)]
60. Bodnar, R.J.; Reynolds, T.J.; Kuehn, C.A. Fluid-Inclusion systematics in epithermal systems. *Rev. Econ. Geol.* **1985**, *2*, 73–97.
61. Díaz-García, M.E.; Badía-Laiño, R. Fluorescence, Derivatization. In *Encyclopedia of Analytical Science*, 2nd ed.; Worsfold, P., Townshend, A., Poole, C., Eds.; Elsevier: Amsterdam, The Netherlands, 2005; pp. 138–148.
62. Wood, S.A.; Shannon, W.M. Rare-earth elements in geothermal waters from Oregon, Nevada, and California. *J. Solid State Chem.* **2003**, *171*, 246–253. [[CrossRef](#)]
63. Sillitoe, R.H. Porphyry copper systems. *Econ. Geol.* **2010**, *105*, 3–41. [[CrossRef](#)]
64. Melfos, V.; Voudouris, P.; Melfou, M.; Sánchez, M.G.; Papadopoulou, L.; Filippidis, A.; Spry, P.G.; Schaarschmidt, A.; Klemm, R.; Haase, K.M.; et al. Mineralogical constraints on the potassic and sodic-calcic hydrothermal alteration and vein-type mineralization of the Maronia porphyry Cu-Mo ± Re ± Au deposit in NE Greece. *Minerals* **2020**, *10*, 182. [[CrossRef](#)]
65. Zhou, Z.; Yonezu, K.; Imai, A.; Tindell, T.; Li, H.; Gabo-Ratio, J.A. Trace elements mineral chemistry of sulfides from the Woxi Au-Sb-W deposit, southern China. *Resour. Geol.* **2021**, *72*, e12279. [[CrossRef](#)]